University of Reading

The global statistical response of the outer radiation belt during geomagnetic storms

Article

Published Version

Creative Commons: Attribution 4.0 (CC-BY)

Open access

Murphy, K. R., Watt, C. E. J., Mann, I. R., Jonathan Rae, I., Sibeck, D. G., Boyd, A. J., Forsyth, C. F., Turner, D. L., Claudepierre, S. G., Baker, D. N., Spence, H. E., Reeves, G. D., Blake, J. B. and Fennell, J. (2018) The global statistical response of the outer radiation belt during geomagnetic storms. Geophysical Research Letters, 45 (9). pp. 3783-3792. ISSN 0094-8276 doi: 10.1002/2017GL076674 Available at https://centaur.reading.ac.uk/76828/

It is advisable to refer to the publisher's version if you intend to cite from the work. See Guidance on citing.

To link to this article DOI: http://dx.doi.org/10.1002/2017GL076674

Publisher: American Geophysical Union

All outputs in CentAUR are protected by Intellectual Property Rights law, including copyright law. Copyright and IPR is retained by the creators or other copyright holders. Terms and conditions for use of this material are defined in the End User Agreement.

www.reading.ac.uk/centaur

University of Reading

CentAUR

Central Archive at the University of Reading

Reading's research outputs online

AGU100 ADVANCING EARTH AND SPACE SCIENCE

Geophysical Research Letters

RESEARCH LETTER
10.1002/2017GL076674

Key Points:
- Statistical assessment of the global and repeatable response of the outer radiation belt to storms
- Using radiation belt content derived from phase space density reduces impacts from adiabatic changes revealing a clear sequence of events
- The statistical response is characterized by a fast genuine-loss dominated phase followed by a clear acceleration phase

Supporting Information:
- Supporting Information S1

Correspondence to:
K. R. Murphy,
kyle.r.murphy@nasa.gov

Citation:
Murphy, K. R., Watt, C. E. J., Mann, I. R., Jonathan Rae, I., Sibeck, D. G., Boyd, A. J., et al. (2018). The global statistical response of the outer radiation belt during geomagnetic storms. *Geophysical Research Letters, 45*. https://doi.org/10.1002/2017GL076674

Received 5 DEC 2017
Accepted 27 MAR 2018
Accepted article online 2 APR 2018

©2018. The Authors.
This is an open access article under the terms of the Creative Commons Attribution License, which permits use, distribution and reproduction in any medium, provided the original work is properly cited.

The Global Statistical Response of the Outer Radiation Belt During Geomagnetic Storms

K. R. Murphy[1,2], C. E. J. Watt[3], I. R. Mann[4], I. Jonathan Rae[5], D. G. Sibeck[1], A. J. Boyd[6], C. F. Forsyth[5], D. L. Turner[7], S. G. Claudepierre[7], D. N. Baker[8], H. E. Spence[9], G. D. Reeves[6,10], J. B. Blake[7], and J. Fennell[7]

[1]NASA Goddard Space Flight Centre, Greenbelt, MD, USA, [2]Department of Astronomy, University of Maryland, College Park, MD, USA, [3]Department of Meteorology, University of Reading, Reading, UK, [4]Department of Physics, University of Alberta, Edmonton, Alberta, Canada, [5]Department of Space and Climate Physics, Mullard Space Science Laboratory, University College London, London, UK, [6]New Mexico Consortium, Los Alamos, NM, USA, [7]Space Sciences Department, The Aerospace Corporation, El Segundo, CA, USA, [8]Laboratory for Atmospheric and Space Physics, University of Colorado Boulder, Boulder, CO, USA, [9]Institute for the Study of Earth, Oceans, and Space, University of New Hampshire, Durham, NH, USA, [10]Space Science and Applications, Los Alamos National Laboratory, Los Alamos, NM, USA

Abstract Using the total radiation belt electron content calculated from Van Allen Probe phase space density, the time-dependent and global response of the outer radiation belt during storms is statistically studied. Using phase space density reduces the impacts of adiabatic changes in the main phase, allowing a separation of adiabatic and nonadiabatic effects and revealing a clear modality and repeatable sequence of events in storm time radiation belt electron dynamics. This sequence exhibits an important first adiabatic invariant (μ)-dependent behavior in the seed (150 MeV/G), relativistic (1,000 MeV/G), and ultrarelativistic (4,000 MeV/G) populations. The outer radiation belt statistically shows an initial phase dominated by loss followed by a second phase of rapid acceleration, while the seed population shows little loss and immediate enhancement. The time sequence of the transition to the acceleration is also strongly μ dependent and occurs at low μ first, appearing to be repeatable from storm to storm.

Plain Language Summary The Earth's outer radiation belt is a region of near-Earth space composed of highly energetic electrons. Typically, the outer radiation belt is in a quiet state; however, during geomagnetic storms the outer radiation belt becomes extremely dynamic. During these storms rapid changes in the number of energetic electrons in the outer radiation belt can lead to satellite failures. Our new research has found a level repeatability in storm time outer radiation belt dynamics not previously appreciated and offers important insights into radiation belt modeling and forecasting. This new work can be used to mitigate the negative effects radiation belt electrons can have on satellite infrastructure.

1. Introduction

The outer radiation belt is a toroidal region of the magnetosphere between ~2 and 7 Earth radii from the center of the Earth populated by trapped electrons with energies from hundreds of 100s of keV to multiple MeV (Mauk et al., 2013). Typically, the outer radiation belt exists in a quiescent state. However, during geomagnetic storms the outer radiation belt becomes increasingly dynamic, at times leading to the filling of the slot region which generally separates the outer from the inner radiation belt (Baker et al., 2004; Loto'aniu et al., 2006), the creation of a third radiation belt (Baker et al., 2013; Mann et al., 2016; Turner et al., 2013; Yuan & Zong, 2013a), and the generation of highly energetic electrons capable of disrupting satellite operations (Baker et al., 1994; Wrenn, 1995). These dynamics are controlled by various loss, acceleration, and transport mechanisms including magnetopause shadowing (West et al., 1972) and wave-particle interactions (Schulz & Lanzerotti, 1974), driven by enhanced storm time solar wind and geomagnetic activity (Murphy et al., 2015; Turner et al., 2012). The overall response of the radiation belt during storms results from a superposition of these processes, culminating in an extremely complex and coupled system. For example, comparisons of prestorm and poststorm fluxes of relativistic electrons at geosynchronous orbit suggest that the dynamics of the outer radiation belt can be difficult to predict based on geomagnetic activity alone (Anderson et al., 2015; Reeves et al., 2003). However, when the dynamics of storm time outer radiation belt electrons are characterized as a function of L shell and electron energy (Turner et al., 2015) or solar wind driver (e.g., Hietala et al.,

2014; Kilpua et al., 2015; Miyoshi & Kataoka, 2005; Yuan & Zong, 2013b), the storm time response is generally more predictable.

Turner et al. (2015) demonstrated that enhancements in the flux of lower-energy electrons (100s of keV) are common during storms, especially at low L shells ($L <$ ~4.6 R_E). Miyoshi and Kataoka (2005) showed that the geosynchronous electron flux tended to be higher during storms driven by corotating interaction regions (CIRs) than those driven by coronal mass ejections (CMEs; c.f., Borovsky & Denton, 2006). Kilpua et al. (2015) demonstrated that storms driven by CME sheath or ejecta were dominated by electron loss. Yuan and Zong (2013b) used low-altitude observations of relativistic electrons to demonstrate that CME-driven storms produce larger radiation belt enhancements at lower L shells than the CIR-driven storms (c.f., Shen et al., 2017). Interestingly, the sum of individual results from these studies does not form a coherent description of the response of the outer radiation belt to geomagnetic storms; rather the radiation belt exhibits a complex response dependent on electron energy, L shell, and storm driver. Here we suggest that a global measure of the energetic electrons in the outer radiation belt, analyzed in a way that normalizes the duration of each important stage in a storm, can provide new information and well-defined patterns in outer radiation belt behavior.

Using Van Allen Probes observations, we characterize the response of the outer radiation belt during 73 storms. Electron phase space density (PSD) and total radiation belt electron content (TRBEC) are used to characterize the radiation belt dynamics as a function of the first and second adiabatic invariants μ and K such that reversible adiabatic effects are removed. Using TRBEC, we demonstrate that storm time electron radiation belt dynamics are statistically characterized sequentially by an initial period dominated by loss followed by a subsequent period dominated by rapid acceleration. Significantly, our results reveal a level of simplicity and repeatability in storm time radiation belt electron dynamics not previously appreciated: the μ dependence of these results being important for understanding the dominant processes which act to shape energetic particle dynamics during storms.

2. Data and Analysis

This study uses data from the Van Allen Probes and OMNIweb (King & Papitashvili, 2005) to statistically characterize the solar wind and response of the radiation belt during 73 geomagnetic storms. We use 52 storms as detailed by Turner et al. (2015) from September 2012 to February 2015, which were identified using a *Sym-H* threshold of −50 nT. These storms are supplemented with 21 storms from February 2015 to March 2016 using the same criteria. These storms are composed of mostly CME-driven storms (~57%). This database (supporting information, Table S1) is used to perform a superposed epoch analysis of storm time radiation belt electron dynamics.

The storm time response of the outer radiation belt is characterized using observations from the Magnetic Electron Ion Spectrometer (MagEIS) (Blake et al., 2013; Claudepierre et al., 2015) and Relativistic Electron Proton Telescope (REPT) (Baker et al., 2012) instruments to calculate the TRBEC (or radiation belt content; Baker et al., 2004). The TRBEC is a proxy for the total number of electrons within the radiation belt and allows the dimensionality of the complex multidimensional MagEIS and REPT data sets to be reduced. TRBEC is ideal for characterizing macroscale changes in the radiation belt for statistical studies (Baker et al., 2004), including the response of the radiation belt to substorms (Forsyth et al., 2016). The TRBEC used here is derived by integrating electron PSD over the three adiabatic invariants, μ, K, and L^*. The PSD f is calculated using the methodology detailed in Boyd et al. (2014), supporting information Text S2. TRBEC N can then be calculated from PSD according to

$$N = \iiint (2\pi)^3 f(\mu, K, L^*) \frac{8\sqrt{2}\pi^2 m_0^{3/2} \mu_0}{R_E} \frac{\sqrt{\mu}}{L^{*2}} d\mu dK dL^* \quad (1)$$

where R_E is the radius of the Earth, m_0 is the mass of an electron, and μ_0 is the permeability of free space. By integrating equation (1) TRBEC can be calculated for different electron energy populations (integral over fixed μ range) and different regions of the outer radiation belt (integral over fixed ranges in K and L^*) while removing reversible adiabatic effects, such as the *Dst* effect (Kim & Chan, 1997).

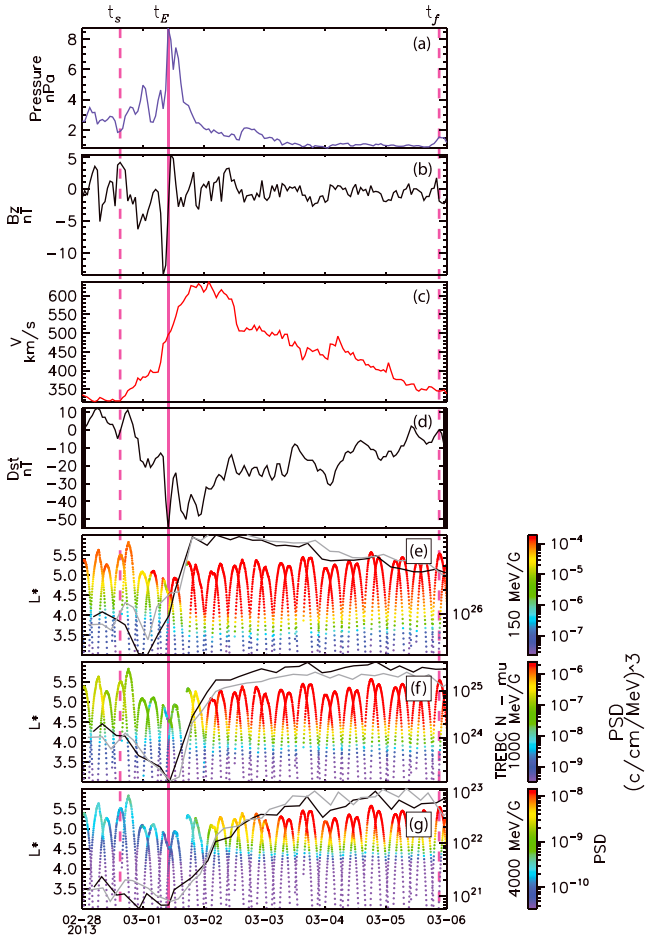

Figure 1. An example geomagnetic storm from 28 February 2013 to 6 March 2013. The dashed lines mark the start and end defined by solar wind driving and geomagnetic activity (t_s and t_f, respectively, as discussed in S1), and the solid line marks the epoch time t_E. (a) Dynamic pressure, (b) B_Z, (c) solar-wind velocity V_{SW}, (d) *DST*. (e–g) The bottom three panels show the PSD at three μ values, μ = 150, 1,000, 4,000 MeV/G, corresponding to the radiation belt seed, relativistic, and ultrarelativistic electron populations, respectively. The dashed and solid black lines in the bottom three panels are the TRBEC N for each μ at fixed $K = 0.1\ R_E G^{1/2}$ from Van Allen A and B, respectively.

In this study PSD is integrated over each half orbit for discrete values of μ and K giving TRBEC $N(\mu, K)$; the lower limit of the integral is $L^* = 3$, and the upper limit is L^* at apogee. Three values of μ are used, μ_1 = 150 MeV/G, μ_2 = 1,000 MeV/G, and μ_3 = 4,000 MeV/G, corresponding to the radiation belt seed, relativistic, and ultrarelativistic electron populations. At $L^* = 5$, μ_1 corresponds to ~300-keV electrons, μ_2 to ~1-MeV electrons, and μ_3 to ~2.5 MeV. Note that the Van Allen Probes is a near-equatorial mission which limits the pitch angle coverage when the probes are off the equator. Hence, we restrict our analysis to $K \in [0.02,0.9]\ R_E G^{1/2}$; outside this range, errors in PSD, and thus TRBEC, can be large. The calculation of TRBEC $N(\mu, K)$ allows the investigation of radiation belt seed, relativistic, and ultrarelativistic electron populations as a function of K (low K corresponding to near-equatorially trapped electrons) across the outer radiation belt (integration of each half orbit in L^*) with adiabatic effects removed.

It is important to note that variation in the strength of the Earth's magnetic field during storms changes the L^* at the apogee of the Van Allen Probes and hence the upper limit of integration over L^*. For instance, during the storm main phase L^* at apogee typically decreases due to compressions of the dayside magnetic field resulting in an increase in the local magnetic field strength (c.f., Figure 1). Thus, while adiabatic effects are removed using PSD, there does exist an unavoidable variation in the integral limits of L^* when calculating TRBEC. Low Earth orbiting satellites, such as Solar Anomalous and Magnetospheric Particle Explorer (SAMPEX) (e.g., Baker et al., 2004), can overcome this limitation. Future work will utilize low Earth orbiting observations to investigate variation in TRBEC over fixed L ranges.

For each storm, three times are independently identified from solar wind and *Dst* to define the start of the storm t_s, the epoch t_E, and the end of the storm t_f. The epoch is taken as the time of minimum *Dst* during each storm. The start of each geomagnetic storm is identified by enhanced solar wind driving, and the end of each storm is determined by recovery of *Dst* following the end of enhanced solar wind driving (see supporting information Text S3 for specific details of the algorithm). These phases correspond most clearly to the definition of the storm main and recovery phases. It is important to note that these two phases are not the same duration for each storm. To perform a superposed epoch analysis, the initial phase of each storm is normalized to 30 hr and the subsequent phase is normalized to 120 hr (e.g., Yokoyama & Kamide, 1997). Hence, our study differs from previous studies which define the start and end of the storm as a fixed number of days pre-epoch and postepoch (e.g., Kataoka & Miyoshi, 2006) or use the time of the maximum electron flux in a fixed number of days pre-epoch and postepoch (e.g., Reeves et al., 2003).

Figure 1 illustrates the identification of the three storm times and evolution of TRBEC during a storm occurring from 28 February to 6 March 2013. Figures 1a–1d show the solar wind dynamic pressure P_{dyn}, north-south component of the interplanetary magnetic field (IMF) B_Z, solar wind velocity V_{SW}, and *Dst*. Figures 1e–1g show the electron PSD at three μ values and the TRBEC for each μ at $K = 0.1\ R_E G^{1/2}$; the smallest value of continuously observed by the Van Allen probes and characteristic of electrons mirroring close to the magnetic equator (Boyd et al., 2016).

In the solar wind, the initial phase of the storm is characterized by negative B_Z and a rapid increase in solar wind dynamic pressure and velocity. P_{dyn} peaks and B_Z minimize during the initial phase of the storm and rapidly approach quiet values ($P_{dyn} < 2$ nPa, $B_Z \sim 0$ nT) during the second phase of the storm. During the second phase V_{SW} continues to grow to a peak of 638 km/s and then decays toward quiet time values over the subsequent 4 days. During the initial phase, *Dst* rapidly decreases until the epoch, reaching a minimum of

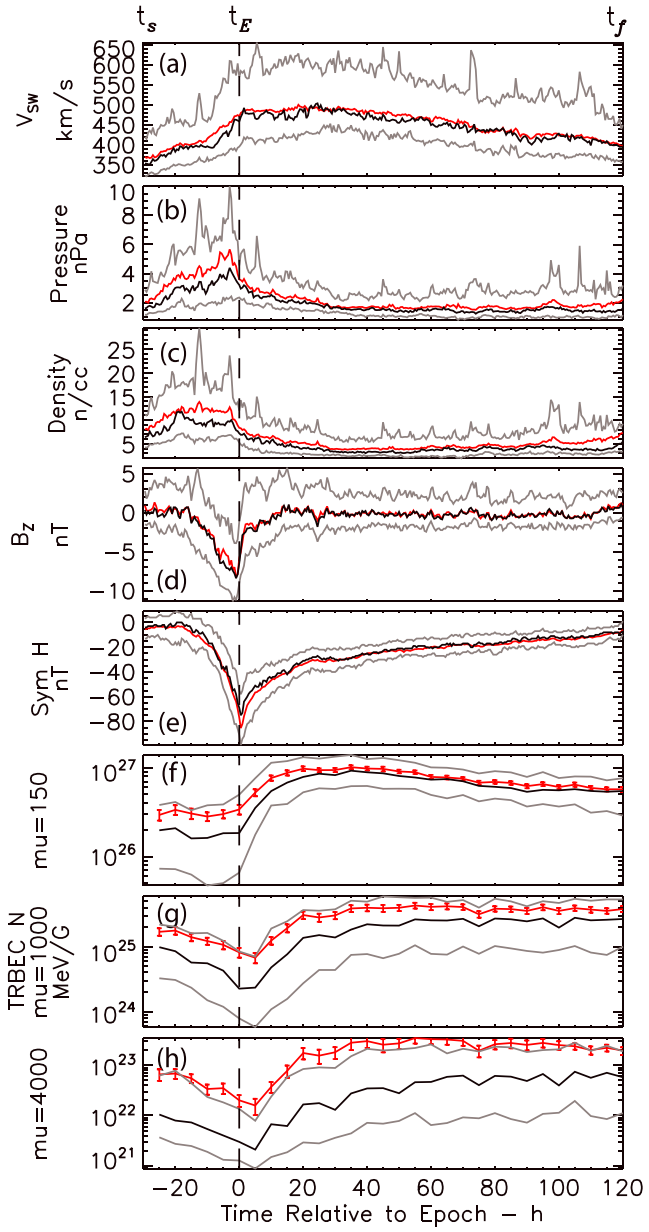

Figure 2. Superposed epoch analysis of solar wind, geomagnetic indices, and TRBEC N. The epoch for each storm is the minimum *Dst*. The start and end of each storm is defined by enhanced solar and geomagnetic conditions. The period from the start of each storm to the epoch is normalized to 30 hr, and the period from the epoch to the end of each storm is normalized to 120 hr. The median is shown in black, mean in red, and upper and lower quartiles in gray. (a) Solar-wind velocity V_{SW}. (b) Dynamic pressure P_{dyn}. (c) Density V_ρ, (d) IMF B_Z. (e) *Sym-H*. (f–h) TRBEC at μ_1 = 150 MeV/G, μ_2 = 1,000 MeV/G, and μ_3 = 4,000 MeV/G and fixed $K = 0.1\ R_E G^{1/2}$. The error bars on the mean total radiation belt electron content (TRBEC) are calculated as the standard deviation of the mean.

−55 nT, and then slowly recovers during the second phase of the storm. During this storm the radiation belt shows a strong and very clear response to solar wind driving. A sharp decrease in both PSD and TRBEC is observed in the initial phase followed by a rapid increase exceeding prestorm values, representing a storm time radiation belt enhancement. Note that despite the limitation in calculating TRBEC over L^*, TRBEC still captures the key dynamics of the geomagnetic storm, in this case an initial period of loss followed by a rapid enhancement of the outer radiation belt. The following sections present results of a superposed epoch analysis of TRBEC and solar wind and discuss the implications of these results for radiation belt dynamics.

3. Results

Figure 2 shows the results of the superposed epoch analysis of the 73 geomagnetic storms. Figures 2a–2d show the V_{SW}, P_{dyn}, density (V_ρ), and B_Z; Figure 2e the geomagnetic index *Sym-H*; and Figures 2f–2h the radiation belt response in TRBEC at the three μ values and fixed $K = 0.1\ R_E G^{1/2}$. In each panel the median is shown in black, mean in red, and upper and lower quartiles in gray. During the initial phase of geomagnetic storms (t_s-t_E) the solar wind shows a monotonic increase in V_{SW} and decrease in B_Z. Solar wind P_{dyn} and V_ρ also show a clear increase though are more dynamic, exhibiting multiple peaks during the initial phase. During this initial phase P_{dyn}, V_ρ, and IMF B_Z reach their most extreme values. Following the initial phase of the geomagnetic storms (t_E-t_f), P_{dyn}, V_ρ, and IMF B_Z rapidly approach quiet values, while V_{SW} continues to increase followed by a slow decay over an extended period. Geomagnetic activity increases as characterized by a rapid decrease in *Sym-H* during the initial phase and slowly approaches quiet values during the second phase. Despite the continued increase in V_{SW} during the second phase, a rapid drop in V_ρ leads to a significant decrease in P_{dyn}. These patterns are consistent in the median, mean, and upper and lower quartiles.

In terms of the dynamics of TRBEC, there is a clear μ-dependent response at fixed $K = 0.1\ R_E G^{1/2}$. During the initial phase, at μ_1, the response of TRBEC is strongly dependent on the quartiles. The lower quartile shows evidence of a small amount of loss, while the median, mean, and upper quartiles remain relatively constant. However, during the second phase the response is very well organized, the quartiles and mean and median values all show a rapid increase in TRBEC. This can be contrasted with the responses at higher μ where each quartile, and indeed almost all of the storms, shows the same behavior. At μ_2 the initial phase is characterized by a systematic net decrease reaching a minimum at the epoch time where it subsequently rapidly enhances during the second phase of the storm. At higher μ, μ_3 shows a similar pattern of net decrease followed by net increase; however, the minimum TRBEC observed is after the epoch time. Hence, the time which acceleration is observed is strongly μ dependent, but at μ_2 and μ_3 almost all storms show the same time sequence of loss and then acceleration across the quartiles. The statistical significance in the variation of TRBEC is tested using the Student's *t* test and the Mann-Whitney-Wilcoxon test which are used to determine if the means and medians of two distributions are statically different, respectively. Comparing the TRBEC distributions at t_{-30} and t_0, and t_0 and t_{30}, using the Student's *t* test and Mann-Whitney-Wilcoxon test demonstrates that the decrease in the

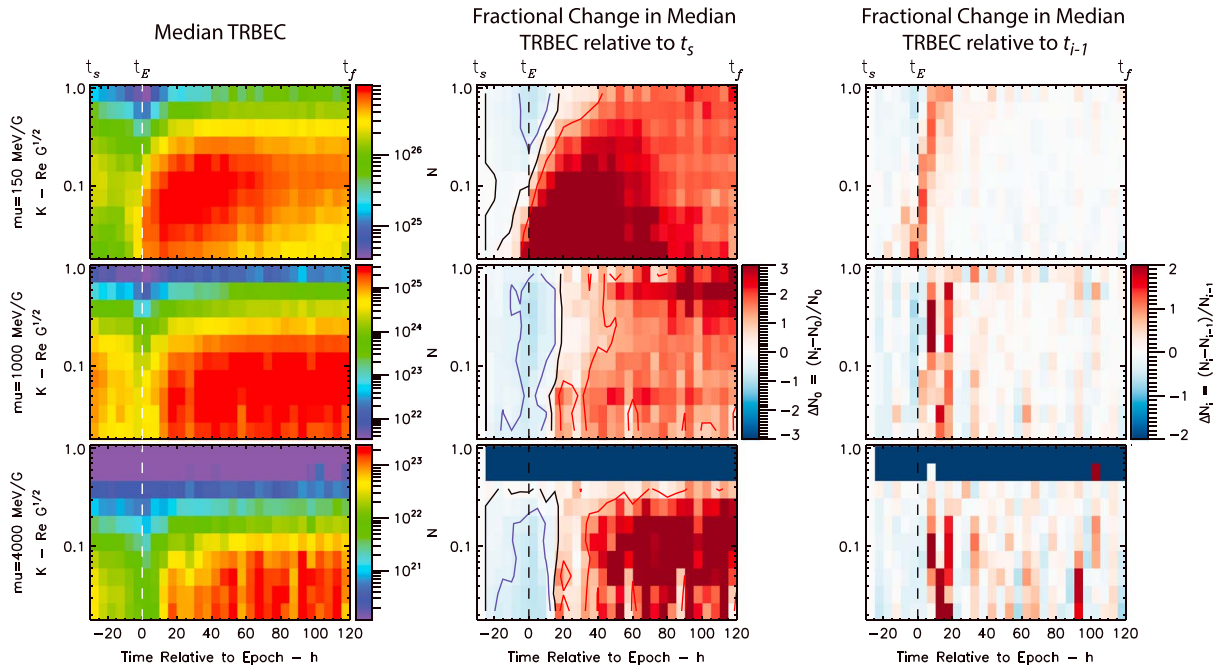

Figure 3. Superposed epoch analysis of total radiation belt electron content (TRBEC) at μ_1 = 150 MeV/G, μ_2 = 1,000 MeV/G, and μ_3 = 4,000 MeV/G (top, middle, and bottom rows, respectively) as a function of the second adiabatic invariant, *K*. Left column, TRBEC. Middle column, fractional change in TRBEC relative to the TRBEC relative to N_0 observed at t_s defined as $\Delta N_0 = (N_i - N_0)/N_0$; the contours in each panel are drawn at $\Delta N_0 = -0.5, 0, 1$ corresponding to a decrease by a factor of 2, no change, and an increase by a factor of 2 in TRBEC relative to the start of the storm (blue, black, and red, respectively). Right column, fractional change in TRBEC as a function of time defined as $\Delta N_i = (N_i - N_{i-1})/N_{i-1}$where the subscript *i* denotes time.

TRBEC in μ_2 and μ_3 during the initial phase and increase in TRBEC across all μ during the second phase are statistically significant to the 99% confidence level.

Figure 3 shows a superposed epoch analysis of TRBEC *N* for the three μ values as a function of *K*. The left column of Figure 3 shows the median value of TRBEC *N* from the superposed epoch analysis, the middle column shows the fractional change of TRBEC *N* relative to N_0 observed at t_s defined as $\Delta N_0 = (N_i - N_0)/N_0$, and the right column shows the fractional change of TRBEC *N* as a function of time $\Delta N_i = (N_i - N_{i-1})/N_{i-1}$, where *i* denotes the time step. Across *K* the response of the radiation belt during storms is remarkably coherent, each μ showing a similar pattern as observed in Figure 2.

At the higher μ and across *K*, the left column of Figure 3 shows that the initial phase of storms is dominated by a net decrease or loss of electrons and the second phase is dominated by a net increase of electrons mediated either by acceleration or transport of electrons. This sequence is most discernible at the higher μ values corresponding to the relativistic (μ_2) and ultrarelativistic (μ_3) electron populations (middle and bottom rows of Figure 3). During the initial phase the TRBEC at these μ values decreases by an order of magnitude (yellow to green) and then rapidly increases by a similar factor (green to red) during the second phase of the storm. At lower μ (top row) the overall behavior of the seed population is different; a decrease during the initial phase is less apparent although a clear enhancement of TRBEC is observed during the second phase. Note the at μ_3 the TRBEC above $K = 0.58\ R_E G^{1/2}$ is nominally zero, due to low count rates at high energies.

The fractional change in TRBEC relative to the start of the storm, ΔN_0 (middle column), depicts periods of a storm during which TRBEC is either smaller, $\Delta N_0 < 0$ (blue), or larger, $\Delta N_0 > 0$ (red), than the initial value of TRBEC. Contours are drawn at $\Delta N_0 = -0.5, 0, 1$ (blue, black, and red) corresponding to a decrease by a factor of 2, no change, and an increase by a factor of 2 in TRBEC relative to the start of the storm. The plots of ΔN_0 as a function of μ and *K* very clearly illustrate the sequence of events discussed above, a net decrease followed by net increase in TRBEC during storms. During the initial phase of storms μ_1 exhibits a relative loss at $K > 0.05\ R_E G^{1/2}$ ($\Delta N_0 < 0$). Below this value of *K* there is a relative increase ($\Delta N_0 < 0$). Note that the

Van Allen Probe orbit does not continuously observe PSD at these values of K, and so we cannot necessarily interpret these changes physically. In contrast, during the second phase $\mu_1$shows a relative increase in TRBEC across the spectrum of K ($\Delta N_0 > 0$). At the higher μs, μ_2 and μ_3, the initial phase and early second phase are characterized by a relative decrease in TRBEC followed by a relative increase from the start of storm. This is characterized by negative values of ΔN_0 (blue) during the initial phase and positive values of ΔN_0 (red) during the second phase of storms. The transition from decreases to increases occurs at t = 10 hr for μ_2 and slightly later at t = 15 hr for μ_3.

The right column of Figure 3 shows the fractional change in TRBEC as a function of time ΔN_i, identifying intervals when electron loss (negative values) or acceleration and transport (positive values) dominate. Three distinct features stand out in ΔN_i. First, each μ is initially characterized by negative ΔN_i (blue) and a net loss of electrons is also illustrated in ΔN_0 (middle column of Figure 3). Second, following an initial period of negative ΔN_i, each μ shows a short period of large and positive ΔN_i (red) characterizing a period of rapid increase in TRBEC across μ and K. The onset of this rapid increase in ΔN_i is also a function of μ, observed initially at μ_1 at $t = -5$ hr, subsequently at μ_2 at t = 0 hr, and finally at μ_3 at t = 5 hr. There is also evidence that this increase is dependent on K, starting initially at lower K and moving to higher values. Finally, following the period of positive ΔN_i, there is a transition to a quasi steady state in TRBEC at $t > 20$ hr for each of μ. This is characterized by small values of ΔN_i that fluctuate between positive and negative.

Overall, Figures 2 and 3 demonstrate three novel aspects of storm time radiation belt electrons. First, the radiation belt has a clear sequence of events responding in a statistically repeatable manner during storms. This response is characterized by an initial period dominated by net decreases followed by a short period of rapid increases in TRBEC. Second, this response is observed across nearly all K at fixed μ demonstrating a coherence in K or pitch angle in this response. Finally, this response is μ dependent; the transition from decreases in TRBEC to increases occurs first for low μ_1 and subsequently for μ_2 and μ_3 or initially in the radiation belt seed population followed by the relativistic and ultrarelativistic populations.

4. Discussion

In this paper we have performed a superposed epoch analysis of the dynamics of the Earth's outer radiation belt during 73 geomagnetic storms observed by the Van Allen Probes predominantly driven by CMEs (57%). The superposed epoch analysis uses electron PSD (Boyd et al., 2016) to calculate the TRBEC (Baker et al., 2004; Forsyth et al., 2016) as a function of the first and second adiabatic invariants. The use of PSD and TRBEC in the superposed epoch analysis has two key advantages for studying storm time electron dynamics. First, PSD removes adiabatic or reversible changes, such as the *Dst* effect, in the derivation of TRBEC. By removing adiabatic effects, changes in TRBEC are the result of *real* changes in the number of outer radiation belt electrons, at least to the extent that this can be monitored across the L^* range observed along the Van Allen Probes orbit. Second, with TRBEC global electron dynamics throughout the outer radiation belt can be investigated as opposed to single point measurements at a fixed L shell.

In the superposed epoch analysis the start of each storm is defined by enhanced solar wind driving, which leads to enhanced geomagnetic activity such as increased ultralow frequency (ULF; e.g., Mathie & Mann, 2001; Murphy et al., 2015) very low frequency (VLF; Aryan et al., 2016), and electromagnetic ion cyclotron (EMIC) wave activity (Halford et al., 2016; Usanova et al., 2012). The epoch time t_E is defined as the minimum in *Dst*, and the end of each storm is defined as the end of enhanced solar wind driving and recovery of *Dst* to nominally quiet values. By characterizing epoch times based on enhanced solar wind and geomagnetic activity, the dynamics of storm time radiation belt electrons can be studied accounting for the varying length of the storm. Further, this analysis provides three independently defined and physics-based epoch times determined from observed quantities associated with enhanced geomagnetic activity and thus enhanced dynamics in radiation belt electrons and TRBEC. These epoch times allow us to cross compare and statistically characterize storm time electron dynamics based on enhanced solar wind driving and geomagnetic activity avoiding the pitfalls when using fixed epochs that can mask patterns.

A clear sequence of events is statistically observed in both the solar wind driving and the response of the three radiation belt electron populations to this driving. During the initial phase of storms V_{SW}, V_ρ, and P_{dyn} rapidly increase and B_Z becomes negative. B_Z, V_ρ, and P_{dyn} reach extreme values during the initial

phase and rapidly approach quiet values during the second phase. V_{SW} peaks during the second phase of storms and subsequently slowly decays. In TRBEC the initial phase is characterized by a net decrease in TRBEC and the second phase is characterized by a net increase in TRBEC across nearly all *K*, especially evident in the relativistic populations. Figures 2 and 3 also show a clear dependence of TRBEC on the first adiabatic invariant μ. Enhancements in TRBEC are first observed at lower μ and later at higher values of μ.

Our observations demonstrate that statistically the global dynamics of the seed, relativistic, and ultrarelativistic populations in the outer radiation belt are not necessarily controlled by a delicate balance of loss and acceleration at any given point during a storm. Rather, these electron populations show a very well defined initial phase dominated by loss (characterized by a net decrease in TRBEC) followed by a short period of rapid acceleration (characterized by a net increase in TRBEC) followed by a transition to either a balance between loss and acceleration or a quiescent period with limited loss and acceleration. This is emphasized in the middle and right columns of Figure 3.

Figure 3 also reveals a very clear coherency in the dynamics of the three radiation belt populations. There is evidence of a time-dependent response in *K*, smaller *K* responding first followed by large *K*; this suggests a pitch angle-dependent response in the recovery which may be mediated by pitch angle-dependent wave-particle interactions (e.g., Li et al., 2014) and will be investigated in detail in future work. Overall, our findings agree with and expand upon previous studies that have separately demonstrated a global coherence in different populations in the outer radiation belt. Kanekal et al. (2001) compared relativistic electron flux observed by Polar at high altitudes with SAMPEX at low altitudes near the footprint of magnetic field lines and found a remarkable global coherence in the dynamics of relativistic electron in the outer radiation belt (see also Baker et al., 2004; Chen et al., 2016). The work here demonstrates that the global coherence of radiation belt electrons exists across the entire outer radiation belt from lower-energy seed electrons up to ultrarelativistic electrons.

The statistical comparison between solar wind and outer radiation belt observations presented here points to a statistically likely and systematic sequence of events controlling storm time radiation belt dynamics. During the initial phase of storms negative B_Z, enhanced dynamic pressure, and a rapid increase in solar wind velocity push the magnetopause inward (Shue et al., 1998; Sibeck et al., 1991) and drive enhanced magnetospheric activity in the form of ULF (Murphy et al., 2015) and VLF (Aryan et al., 2016) waves. The inward motion of the magnetopause leads to the rapid loss of radiation belt electrons via magnetopause shadowing (Ozeke et al., 2014; Turner et al., 2012) further enhanced by outward radial diffusion via ULF waves (Mann et al., 2016; Murphy et al., 2015; Ozeke et al., 2014) and precipitation driven by enhanced EMIC (Usanova et al., 2012) and VLF wave activity (Orlova et al., 2014).

During the second phase of the storm B_Z, V_ρ, and P_{dyn} decay toward quiet values. As a result, the magnetopause begins to withdraw retreating away from the Earth and the outer radiation belt and loss via magnetopause shadowing is reduced. At this point, the outer radiation belt transitions from a period dominated by loss to a short period dominated by a rapid enhancement in the radiation belt seed, relativistic, and ultrarelativistic populations. During the second phase, V_{SW} peaks and slowly decays, providing a mechanism for enhanced ULF wave power during the second phase of geomagnetic storms (Mathie & Mann, 2001; Murphy et al., 2011; Pahud et al., 2009; Rae et al., 2012). In terms of radiation belt dynamics, the electron seed population is the first to recover during the second phase of storms. This recovery is likely via the injection of low-energy electrons via substorms driven by the release of nightside energy stored via reconnection and negative B_Z during the initial phase of storms (e.g., Baker et al., 1998; Jaynes et al., 2015). These substorms also drive enhanced VLF (Meredith et al., 2004) and ULF (Murphy et al., 2011; Rae et al., 2011) activities. The recovery of the seed population of electrons and enhanced ULF and VLF wave activities subsequently leads to recovery of the relativistic and ultrarelativistic electron populations via radial diffusion (e.g., Li et al., 2017; Mann et al., 2016; Ozeke et al., 2012, 2017; Shprits et al., 2005; Su et al., 2015) and local acceleration (e.g., Horne et al., 2005; Li et al., 2014; Reeves et al., 2013; Thorne et al., 2013). A key feature of the second phase of storms is the rapid enhancement of the three electron populations as opposed to a slow or gradual recovery. Any theory or modeling of radiation belt dynamics must be able to reproduce this rapid enhancement during storms. Future work will concentrate on studying the physical processes occurring during this phase of storms and attempts to distinguish between the causality of the possible mechanisms leading to this rapid enhancement in radiation belt electron fluxes.

5. Conclusions

Our superposed epoch analysis represents a refocusing of radiation belt research, demonstrating that statistically, storm time radiation belt dynamics throughout the entire outer radiation belt are repeatable. This repeatability is characterized by an enhanced solar wind driving which leads to rapid loss at the start of a storm followed by a rapid enhancement in the outer radiation belt seed, relativistic, and ultrarelativistic electron populations during storms. Future work will exploit this response and separation of electron dynamics into an initial phase dominated by loss followed by a second phase dominated by acceleration to attempt to quantify the causality and the importance of the role of various loss (e.g., Millan & Thorne, 2007; Turner et al., 2012) and acceleration processes (e.g., Elkington, 2006; Horne et al., 2006; Mann et al., 2012; Thorne, 2010) in the dynamics of electrons during geomagnetic storms as well as extend the analysis into solar minimum, a period dominated by CIR-driven storms as opposed to CME-driven storms as studied here.

Acknowledgments

Work by K. R. M., D. G. S., and D. L. T. are partially supported by the Van Allen Probes mission. C. E. J. W. is supported by STFC grant ST/M000885/1 and NERC grant NE/P017274/1. I. R. M. is supported by a Discovery Grant from Canadian NSERC. I. J. R. is supported in part by STFC grant ST/N000722/1 and by NERC grants NE/L007495/1, NE/P017150/1, and NE/P017185/1. This work was also supported by RBSP-ECT funding provided by JHU/APL contract 967399 under NASA's Prime contract NAS5-01072. Work at JHU/APL was supported by NASA grant NNX10AK93G. Van Allen MagEIS, REPT, and ephemeris data are available at https://www.rbsp-ect.lanl.gov; solar wind data are available through OMNIweb at https://omniweb.gsfc.nasa.gov/. Van Allen PSD can be calculated from the background-corrected MagEIS and REPT electron fluxes as outlined in Boyd et al. (2014) and is also available upon request.

References

Anderson, B. R., Millan, R. M., Reeves, G. D., & Friedel, R. H. W. (2015). Acceleration and loss of relativistic electrons during small geomagnetic storms. *Geophysical Research Letters*, *42*, 10,113–10,119. https://doi.org/10.1002/2015GL066376

Aryan, H., Sibeck, D., Balikhin, M., Agapitov, O., & Kletzing, C. (2016). Observation of chorus waves by the Van Allen Probes: Dependence on solar wind parameters and scale size. *Journal of Geophysical Research: Space Physics*, *121*, 7608–7621. https://doi.org/10.1002/2016JA022775

Baker, D., Kanekal, S. G., Hoxie, V. C., Batiste, S., Bolton, M., & Li, X. (2012). The relativistic electron-proton telescope (REPT) instrument on board the radiation belt storm probes (RBSP) spacecraft: Characterization of Earth's radiation belt high-energy particle populations. *Space Science Reviews*, *179*(1-4), 337–381. https://doi.org/10.1007/s11214-012-9950-9

Baker, D. N., Kanekal, S., Blake, J. B., Klecker, B., & Rostoker, G. (1994). Satellite anomalies linked to electron increase in the magnetosphere. *EOS. Transactions of the American Geophysical Union*, *75*(35), 401. https://doi.org/10.1029/94EO01038

Baker, D. N., Kanekal, S. G., & Blake, J. B. (2004). Characterizing the Earth's outer Van Allen zone using a radiation belt content index. *Space Weather*, *2*, S02003. https://doi.org/10.1029/2003SW000026

Baker, D. N., Kanekal, S. G., Hoxie, V. C., Henderson, M. G., Li, X., Spence, H. E., et al. (2013). A long-lived relativistic electron storage ring embedded in Earth's outer Van Allen belt. *Science*, *340*(6129), 186–190. https://doi.org/10.1126/science.1233518

Baker, D. N., Kanekal, S. G., Li, X., Monk, S. P., Goldstein, J., & Burch, J. L. (2004). An extreme distortion of the Van Allen belt arising from the 'Hallowe'en' solar storm in 2003. *Nature*, *432*, 878–881.

Baker, D. N., Li, X., Blake, J. B., & Kanekal, S. (1998). Strong electron acceleration in the Earth's magnetosphere. *Advances in Space Research*, *21*(4), 609–613. https://doi.org/10.1016/s0273-1177(97)00970-8

Blake, J. B., Carranza, P. A., Claudepierre, S. G., Clemmons, J. H., Crain, W. R., Dotan, Y., et al. (2013). The Magnetic Electron Ion Spectrometer (MagEIS) instruments aboard the Radiation Belt Storm Probes (RBSP) spacecraft. *Space Science Reviews*, *179*(1-4), 383–421. https://doi.org/10.1007/s11214-013-9991-8

Borovsky, J. E., & Denton, M. H. (2006). Differences between CME-driven storms and CIR-driven storms. *Journal of Geophysical Research*, *111*, A07S08. https://doi.org/10.1029/2005JA011447

Boyd, A. J., Spence, H. E., Claudepierre, S. G., Fennell, J. F., Blake, J. B., Baker, D. N., et al. (2014). Quantifying the radiation belt seed population in the 17 March 2013 electron acceleration event. *Geophysical Research Letters*, *41*, 2275–2281. https://doi.org/10.1002/2014GL059626

Boyd, A. J., Spence, H. E., Huang, C. L., Reeves, G. D., Baker, D. N., Turner, D. L., et al. (2016). Statistical properties of the radiation belt seed population. *Journal of Geophysical Research: Space Physics*, *121*, 7636–7646. https://doi.org/10.1002/2016JA022652

Chen, Y., Reeves, G. D., Cunningham, G. S., Redmon, R. J., & Henderson, M. G. (2016). Forecasting and remote sensing outer belt relativistic electrons from low Earth orbit. *Geophysical Research Letters*, *43*, 1031–1038. https://doi.org/10.1002/2015GL067481

Claudepierre, S. G., O'Brien, T. P., Blake, J. B., Fennell, J. F., Roeder, J. L., Clemmons, J. H., et al. (2015). A background correction algorithm for Van Allen Probes MagEIS electron flux measurements. *Journal of Geophysical Research: Space Physics*, *120*, 5703–5727. https://doi.org/10.1002/2015JA021171

Elkington, S. R. (2006). A review of ULF interactions with radiation belt electrons. In K. Takahashi, et al. (Eds.), *Magnetospheric ULF waves: Synthesis and new directions*. Washington, DC: American Geophysical Union. https://doi.org/10.1029/169GM12

Forsyth, C., Rae, I. J., Murphy, K. R., Freeman, M. P., Huang, C. L., Spence, H. E., et al. (2016). What effect do substorms have on the content of the radiation belts? *Journal of Geophysical Research: Space Physics*, *121*, 6292–6306. https://doi.org/10.1002/2016JA022620

Halford, A. J., Fraser, B. J., Morley, S. K., Elkington, S. R., & Chan, A. A. (2016). Dependence of EMIC wave parameters during quiet, geomagnetic storm, and geomagnetic storm phase times. *Journal of Geophysical Research: Space Physics*, *121*, 6277–6291. https://doi.org/10.1002/2016JA022694

Hietala, H., Kilpua, E. K. J., Turner, D. L., & Angelopoulos, V. (2014). Depleting effects of ICME-driven sheath regions on the outer electron radiation belt. *Geophysical Research Letters*, *41*, 2258–2265. https://doi.org/10.1002/2014GL059551

Horne, R. B., Meredith, N. P., Glauert, S. A., Varotsou, A., Boscher, D., Thorne, R. M., et al. (2006). Mechanisms for the acceleration of radiation belt electrons. In B. Tsurutani, et al. (Eds.), *Recurrent magnetic storms: Corotating solar wind streams*. Washington, DC: American Geophysical Union. https://doi.org/10.1029/167GM14

Horne, R. B., Thorne, R. M., Shprits, Y. Y., Meredith, N. P., Glauert, S. A., Smith, A. J., et al. (2005). Wave acceleration of electrons in the Van Allen radiation belts. *Nature*, *437*(7056), 227–230. https://doi.org/10.1038/nature03939

Hutchinson, J. A., Wright, D. M., & Milan, S. E. (2011). Geomagnetic storms over the last solar cycle: A superposed epoch analysis. *Journal of Geophysical Research*, *116*, A09211. https://doi.org/10.1029/2011JA016463

Jaynes, A. N., Baker, D. N., Singer, H. J., Rodriguez, J. V., Loto'aniu, T. M., Ali, A. F., et al. (2015). Source and seed populations for relativistic electrons: Their roles in radiation belt changes. *Journal of Geophysical Research: Space Physics*, *120*, 7240–7254. https://doi.org/10.1002/2015JA021234

Kanekal, S. G., Baker, D. N., & Blake, J. B. (2001). Multisatellite measurements of relativistic electrons: Global coherence. *Journal of Geophysical Research*, *106*(A12), 29,721–29,732. https://doi.org/10.1029/2001JA000070

Kataoka, R., & Miyoshi, Y. (2006). Flux enhancement of radiation belt electrons during geomagnetic storms driven by coronal mass ejections and corotating interaction regions. *Space Weather*, *4*, S09004. https://doi.org/10.1029/2005SW000211

Kilpua, E. K. J., Hietala, H., Koskinen, H. E. J., Fontaine, D., & Turc, L. (2013). Magnetic field and dynamic pressure ULF fluctuations in coronal-mass-ejection-driven sheath regions. *Annales de Geophysique*, *31*, 1559–1567. https://doi.org/10.5194/angeo-31-1559-2013

Kilpua, E. K. J., Hietala, H., Turner, D. L., Koskinen, H. E. J., Pulkkinen, T. I., Rodriguez, J. V., et al. (2015). Unraveling the drivers of the storm-time radiation belt response. *Geophysical Research Letters*, *42*, 3076–3084. https://doi.org/10.1002/2015GL063542

Kim, H. J., & Chan, A. A. (1997). Fully adiabatic changes in storm time relativistic electron fluxes. *Journal of Geophysical Research*, *102*(A10), 22,107–22,116. https://doi.org/10.1029/97JA01814

King, J. H., & Papitashvili, N. E. (2005). Solar wind spatial scales in and comparisons of hourly Wind and ACE plasma and magnetic field data. *Journal of Geophysical Research*, *110*, A02104. https://doi.org/10.1029/2004JA010649

Li, W., Thorne, R. M., Ma, Q., Ni, B., Bortnik, J., Baker, D. N., et al. (2014). Radiation belt electron acceleration by chorus waves during the 17 March 2013 storm. *Journal of Geophysical Research: Space Physics*, *119*, 4681–4693. https://doi.org/10.1002/2014JA019945

Li, Z., Hudson, M., Patel, M., Wiltberger, M., Boyd, A., & Turner, D. (2017). ULF wave analysis and radial diffusion calculation using a global MHD model for the 17 March 2013 and 2015 storms. *Journal of Geophysical Research: Space Physics*, *122*, 7353–7363. https://doi.org/10.1002/2016JA023846

Loto'aniu, T. M., Mann, I. R., Ozeke, L. G., Chan, A. A., Dent, Z. C., & Milling, D. K. (2006). Radial diffusion of relativistic electrons into the radiation belt slot region during the 2003 Halloween geomagnetic storms. *Journal of Geophysical Research*, *111*, A04218. https://doi.org/10.1029/2005JA011355

Mann, I. R., Murphy, K. R., Ozeke, L. G., Rae, I. J., Milling, D. K., Kale, A. A., & Honary, F. F. (2012). The role of ultralow frequency waves in radiation belt dynamics. In D. Summers, et al. (Eds.), *Dynamics of the Earth's radiation belts and inner magnetosphere*. Washington, DC: American Geophysical Union. https://doi.org/10.1029/2012GM001349

Mann, I. R., Ozeke, L. G., Murphy, K. R., Claudepierre, S. G., Turner, D. L., Baker, D. N., et al. (2016). Explaining the dynamics of the ultra-relativistic third Van Allen radiation belt. *Nature Physics*, *12*(10), 978–983. https://doi.org/10.1038/nphys3799

Mathie, R. A., & Mann, I. R. (2001). On the solar wind control of Pc5 ULF pulsation power at mid-latitudes: Implications for MeV electron acceleration in the outer radiation belt. *Journal of Geophysical Research*, *106*(A12), 29,729–29,783. https://doi.org/10.1029/2001JA000002

Mauk, B. H., Fox, N. J., Kanekal, S. G., Kessel, R. L., Sibeck, D. G., & Ukhorskiy, A. (2013). Science objectives and rationale for the radiation belt storm probes mission. *Space Science Reviews*, *179*(1–4), 3–27. https://doi.org/10.1007/s11214-012-9908-y

Meredith, N. P., Horne, R. B., Thorne, R. M., Summers, D., & Anderson, R. R. (2004). Substorm dependence of plasmaspheric hiss. *Journal of Geophysical Research*, *109*, A06209. https://doi.org/10.1029/2004JA010387

Millan, R. M., & Thorne, R. M. (2007). Review of radiation belt relativistic electron losses. *Journal of Atmospheric and Solar - Terrestrial Physics*, *69*(3), 362–377. https://doi.org/10.1016/j.jastp.2006.06.019

Miyoshi, Y., & Kataoka, R. (2005). Ring current ions and radiation belt electrons during geomagnetic storms driven by coronal mass ejections and corotating interaction regions. *Geophysical Research Letters*, *32*, L211105. https://doi.org/10.1029/2005GL024590

Miyoshi, Y., Kataoka, R., Kasahara, Y., Kumamoto, A., Nagai, T., & Thomsen, M. F. (2013). High-speed solar wind with southward interplanetary magnetic field causes relativistic electron flux enhancement of the outer radiation belt via enhanced condition of whistler waves. *Geophysical Research Letters*, *40*, 4520–4525. https://doi.org/10.1002/grl.50916

Murphy, K. R., Mann, I. R., Jonathan Rae, I., & Milling, D. K. (2011). Dependence of ground-based Pc5 ULF wave power on F10.7 solar radio flux and solar cycle phase. *Journal of Atmospheric and Solar - Terrestrial Physics*, *73*(11–12), 1500–1510. https://doi.org/10.1016/j.jastp.2011.02.018

Murphy, K. R., Mann, I. R., & Sibeck, D. G. (2015). On the dependence of storm time ULF wave power on magnetopause location: Impacts for ULF wave radial diffusion. *Geophysical Research Letters*, *42*, 9676–9684. https://doi.org/10.1002/2015GL066592

Murphy, K. R., Rae, I. J., Mann, I. R., & Milling, D. K. (2011). On the nature of ULF wave power during nightside auroral activations and sub-storms: 1. Spatial distribution. *Journal of Geophysical Research*, *116*, A00I21. https://doi.org/10.1029/2010JA015757

Orlova, K., Spasojevic, M., & Shprits, Y. (2014). Activity-dependent global model of electron loss inside the plasmasphere. *Geophysical Research Letters*, *41*, 3744–3751. https://doi.org/10.1002/2014GL060100

Ozeke, L. G., Mann, I. R., Murphy, K. R., Rae, I. J., & Chan, A. A. (2012). ULF wave-driven radial diffusion simulations of the outer radiation belt. *Geophysical Monograph Series*, *199*, 139–149. https://doi.org/10.1029/2012GM001332

Ozeke, L. G., Mann, I. R., Murphy, K. R., Sibeck, D. G., & Baker, D. N. (2017). Ultra-relativistic radiation belt extinction and ULF wave radial diffusion: Modeling the September 2014 extended dropout event. *Geophysical Research Letters*, *44*, 2624–2633. https://doi.org/10.1002/2017GL072811

Ozeke, L. G., Mann, I. R., Turner, D. L., Murphy, K. R., Degeling, A. W., Rae, I. J., & Milling, D. K. (2014). Modeling cross L shell impacts of magnetopause shadowing and ULF wave radial diffusion in the Van Allen belts. *Geophysical Research Letters*, *41*, 6556–6562. https://doi.org/10.1002/2014GL060787

Pahud, D. M., Rae, I. J., Mann, I. R., Murphy, K. R., & Amalraj, V. (2009). Ground-based Pc5 ULF wave power: Solar wind speed and MLT dependence. *Journal of Atmospheric and Solar - Terrestrial Physics*, *71*(10–11), 1082–1092. https://doi.org/10.1016/j.jastp.2008.12.004

Rae, I. J., Mann, I. R., Murphy, K. R., Ozeke, L. G., Milling, D. K., Chan, A. A., et al. (2012). Ground-based magnetometer determination of in situ Pc4-5 ULF electric field wave spectra as a function of solar wind speed. *Journal of Geophysical Research*, *117*, A04221. https://doi.org/10.1029/2011JA017335

Rae, I. J., Murphy, K. R., Watt, C. E. J., & Mann, I. R. (2011). On the nature of ULF wave power during nightside auroral activations and substorms: 2. Temporal evolution. *Journal of Geophysical Research*, *116*, A00I22. https://doi.org/10.1029/2010JA015762

Reeves, G. D., McAdams, K. L., Friedel, R. H. W., & O'Brien, T. P. (2003). Acceleration and loss of relativistic electrons during geomagnetic storms. *Geophysical Research Letters*, *30*(10), 1529. https://doi.org/10.1029/2002GL016513

Reeves, G. D., Spence, H. E., Henderson, M. G., Morley, S. K., Friedel, R. H. W., Funsten, H. O., et al. (2013). Electron acceleration in the heart of the Van Allen radiation belts. *Science*, *341*(6149), 991–994. https://doi.org/10.1126/science.1237743

Schulz, M., & Lanzerotti, L. J. (1974). *Particle diffusion in the radiation belts, physics and chemistry in space* (7th ed., p. 215). New York: Springer-Verlag.

Shen, X.-C., Hudson, M. K., Jaynes, A., Shi, Q., Tian, A., Claudepierre, S., et al. (2017). Statistical study of the storm time radiation belt evolution during Van Allen Probes era: CME- versus CIR-driven storms. *Journal of Geophysical Research: Space Physics*, *122*, 8327–8339. https://doi.org/10.1002/2017JA024100

Shprits, Y. Y., Thorne, R. M., Reeves, G. D., & Friedel, R. (2005). Radial diffusion modeling with empirical lifetimes: COMPARISON with CRRES observations. *Annales de Geophysique*, *23*, 1467–1471.

Shue, J.-H., Song, P., Russell, C. T., Steinberg, J. T., Chao, J. K., Zastenker, G., et al. (1998). Magnetopause location under extreme solar wind conditions. *Journal of Geophysical Research*, *103*(A8), 17,691–17,700. https://doi.org/10.1029/98JA01103

Sibeck, D. G., Lopez, R. E., & Roelof, E. C. (1991). Solar wind control of the magnetopause shape, location, and motion. *Journal of Geophysical Research*, *96*(A4), 5489. https://doi.org/10.1029/90JA02464

Su, Z., Zhu, H., Xiao, F., Zong, Q. G., Zhou, X. Z., Zheng, H., et al. (2015). Ultra-low-frequency wave-driven diffusion of radiation belt relativistic electrons. *Nature Communications*, *6*(1), 10096. https://doi.org/10.1038/ncomms10096

Thorne, R. M. (2010). Radiation belt dynamics: The importance of wave-particle interactions. *Geophysical Research Letters*, *37*, L22107. https://doi.org/10.1029/2010GL044990

Thorne, R. M., Li, W., Ni, B., Ma, Q., Bortnik, J., Chen, L., et al. (2013). Rapid local acceleration of relativistic radiation-belt electrons by magnetospheric chorus. *Nature*, *504*, 411–414. https://doi.org/10.1038/nature12889

Tsyganenko, N. A., & Sitnov, M. I. (2005). Modeling the dynamics of the inner magnetosphere during strong geomagnetic storms. *Journal of Geophysical Research*, *110*, A03208. https://doi.org/10.1029/2004JA010798

Turner, D. L., Angelopoulos, V., Li, W., Hartinger, M. D., Usanova, M., Mann, I. R., et al. (2013). On the storm-time evolution of relativistic electron phase space density in Earth's outer radiation belt. *Journal of Geophysical Research: Space Physics*, *118*, 2196–2212. https://doi.org/10.1002/jgra.50151

Turner, D. L., Morley, S. K., Miyoshi, Y., Ni, B., & Huang, C. L. (2012). Outer radiation belt flux dropouts: Current understanding and unresolved questions. *Geophysical Monograph Series*, *199*, 195–212. https://doi.org/10.1029/2012GM001310

Turner, D. L., O'Brien, T. P., Fennell, J. F., Claudepierre, S. G., Blake, J. B., Kilpua, E. K. J., & Hietala, H. (2015). The effects of geomagnetic storms on electrons in Earth's radiation belts. *Geophysical Research Letters*, *42*, 9176–9184. https://doi.org/10.1002/2015GL064747

Turner, D. L., Shprits, Y., Hartinger, M., & Angelopoulos, V. (2012). Explaining sudden losses of outer radiation belt electrons during geomagnetic storms. *Nature Physics*, *8*(3), 208–212. https://doi.org/10.1038/nphys2185

Usanova, M. E., Mann, I. R., Bortnik, J., Shao, L., & Angelopoulos, V. (2012). THEMIS observations of electromagnetic ion cyclotron wave occurrence: Dependence on AE, SYMH, and solar wind dynamic pressure. *Journal of Geophysical Research*, *117*, A10218. https://doi.org/10.1029/2012JA018049

West, H. I., Buck, R. M., & Walton, J. R. (1972). Shadowing of electron azimuthal-drift motions near the noon magnetopause. *Nature Physical Science*, *240*(97), 6–7. https://doi.org/10.1038/physci240006a0

Wrenn, G. L. (1995). Conclusive evidence for internal dielectric charging anomalies on geosynchronous communications spacecraft. *Journal of Spacecraft and Rockets*, *32*(3), 514–520. https://doi.org/10.2514/3.26645

Yokoyama, N., & Kamide, Y. (1997). Statistical nature of geomagnetic storms. *Journal of Geophysical Research*, *102*(A7), 14215. https://doi.org/10.1029/97JA00903

Yuan, C., & Zong, Q. G. (2013a). The double-belt outer radiation belt during CME- and CIR-driven geomagnetic storms. *Journal of Geophysical Research: Space Physics*, *118*, 6291–6301. https://doi.org/10.1002/jgra.50564

Yuan, C. J., & Zong, Q.-G. (2013b). Relativistic electron fluxes dropout in the outer radiation belt under different solar wind conditions. *Journal of Geophysical Research: Space Physics*, *118*, 7545–7556. https://doi.org/10.1002/2013JA019066